

УДК 551.463.5

© А. А. Мольков^{1,2*}

¹Институт физики атмосферы им. А.М. Обухова РАН, 119017, Пыжевский пер., д. 3, г. Москва, Россия

²Институт прикладной физики РАН, 603950, ул. Ульянова, д. 46. г. Нижний Новгород, Россия

*E-mail: a.molkov@inbox.ru

ПРОЯВЛЕНИЕ ПЛЕНОК ПОВЕРХНОСТНО-АКТИВНЫХ ВЕЩЕСТВ В ИЗОБРАЖЕНИИ КРУГА СНЕЛЛИУСА: ЧИСЛЕННЫЙ ЭКСПЕРИМЕНТ

Статья поступила в редакцию 17.02.2021, после доработки 28.04.2021

Настоящая работа продолжает цикл работ по исследованию возможностей использования подводных изображений небосвода (круга Снеллиуса) для оценки состояния взволнованной водной поверхности, в том числе в поле приповерхностных гидрофизических процессов и в присутствии пленочных загрязнителей. На основе разработанных ранее математических моделей изображений круга Снеллиуса и его первых двух статистических моментов, а также модели спектра ветрового волнения Эльфохейли, модели тонкой пленки Ермакова и эмпирических результатов Кокса-Манка для толстой пленки продемонстрирована чувствительность структуры границы круга Снеллиуса к изменениям ветроволновой обстановки и к пленкам различных вязкоупругих характеристик. Полученные теоретические результаты подкреплены результатами анализа изображений из натурального эксперимента, когда искусственный пленочный слик пересекал область визирования, оказывая заметное влияние на структуру волнения. На основе полученных результатов сформулированы практические возможности обнаружения поверхностных загрязнителей и их различения с проявлениями на водной поверхности других процессов, например, ветровой тенью.

Ключевые слова: дистанционное зондирование, подводное видение, круг Снеллиуса, ветровое волнение, уклоны поверхности, пленки поверхностно-активных веществ, слики.

© А. А. Molkov^{1,2*}

¹A.M. Obukhov Institute of Atmospheric Physics, RAS, 119017, Pyzhyovskiy Per., 3, Moscow, Russia

²Institute of Applied Physics, RAS, 603950, Ulyanova Str., 46, Nizhny Novgorod, Russia

*E-mail: a.molkov@inbox.ru

MANIFESTATION OF SURFACTANT FILM IN SNELL'S WINDOW IMAGE: NUMERICAL EXPERIMENT

Received 17.02.2021, in final form 28.04.2021

The present paper continues a series of studies on using underwater images of the sky (Snell's window) to retrieve characteristics of wind-driven waves and their variations in the field of near-surface hydrophysical processes and under influence of surfactant films. Research is based on the previously developed mathematical models of the Snell's window image and two statistical moments, the Elfouhaily spectrum of wind-driven waves, the Ermakov model of wave damping by a thin film, and the Cox-Munk result for a thick oil film. Varying wind, wave, and film parameters in the numerical experiment, we demonstrated a sensitivity of considered statistical moments to changes in wind-wave conditions and viscoelastic characteristics of films. To distinguish film influence from wind weakening having similar manifestations, a series of real underwater images demonstrating the changes in the spot structure with the passing surfactant film through the observed sea surface area were analyzed. The obtained results demonstrate that presented method can be useful in practice for detecting surfactant films with the help of optical recorders fixed under the buoys, for example.

Key words: remote sensing, underwater imagery, Snell's window, sea roughness, wind waves, wave spectra, slope variance, surfactant film, slick.

1. Introduction

The underwater sky image, or the Snell's window image, is a contrasting object frequently observed in photos of professional and amateur divers (Fig. 1). However, the use of such images to solve scientific problems has not been

Ссылка для цитирования: Мольков А.А. Проявление пленок поверхностно-активных веществ в изображении круга Снеллиуса: численный эксперимент // *Фундаментальная и прикладная гидрофизика*. 2021. Т. 14, № 3. С. 98—110. doi: 10.7868/S2073667321030096

For citation: Molkov A.A. Manifestation of Surfactant Film in Snell's Window Image: Numerical Experiment. *Fundamentalnaya i Prikladnaya Gidrofizika*. 2021, 13, 3, 98—110. doi: 10.7868/S2073667321030096

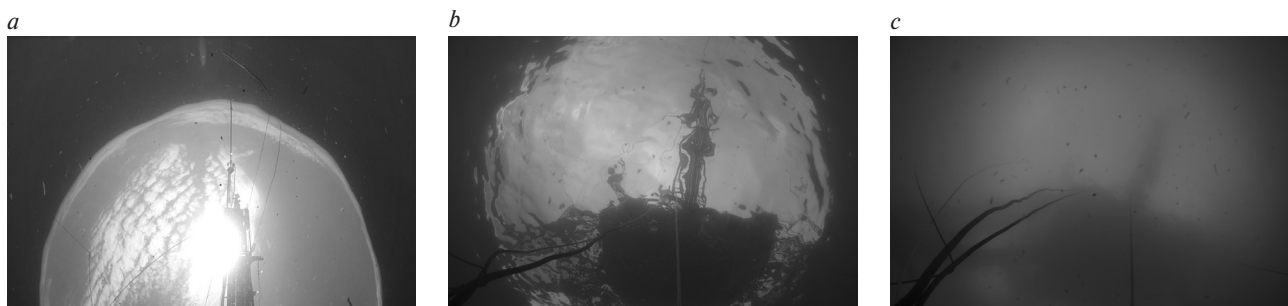


Fig. 1. The Snell's window images obtained from the oceanographic platform in the Black Sea for a flat sea surface from a depth of 0.5 m (*a*) and a rough sea surface from depths of 1.5 m (*b*) and 5 m (*c*) (attenuation coefficient is about 0.6 m^{-1}).

noticed until recently. For a flat sea surface, the Snell's window looks like a light circle with an angular radius equal to the angle of total internal reflection of 48.75° (Fig. 1, *a*). An apparent radiance at bigger angles is determined through the upwelling light reflected by the sea surface to the lower hemisphere. This radiance is too low in comparison with the downwelling one, therefore apparent radiance beyond Snell's window seems comparatively low. Surface waves randomly distort Snell's window border leading appearance of dark and light spots (Fig. 1, *b*). Their contours outline facets where the slope exceeds a certain value depending on spot location. Therefore, estimation of the Snell's window border distortions opened possibilities to retrieve wavy surface characteristics [1]. The latter changes in the field of hydro-physical processes (like internal waves, inhomogeneous flows, etc.), in fetch-limited areas or under the damping of surfactant films. The effect of films is especially interesting in connection with the development of tools for reliable film detection and remote assessment of its characteristics because used methods are still far from this [2–5]. Among the methods indicated in the cited literature, the methods based on image analysis are the closest to the present study. Among them, satellite imagery plays a special role. Now they are actively used to detect rather thick films, estimate cover area, and predict spread direction. Using information in the channels of the long infrared (IR) range ($8\text{--}14 \mu\text{m}$), it is possible to obtain preliminary estimates of the thickness and map of the contamination area by film thickness [4, 6]. However, the observed contrast depends on the daytime, water temperature, and other factors. Water surface monitoring systems in the ranges of $750\text{--}1400 \text{ nm}$ (near IR range, NIR) and $1400\text{--}3000 \text{ nm}$ (mid IR range, MWIR) are used to assess the thickness of films and oil emulsions in a wide range. The key element here is the minima of the film radiance spectra corresponding to absorption bands which are related with the vibrational motions of carbon and hydrogen molecules in oil films and oil emulsions [7, 8]. The conversion of thicknesses to absolute units is possible to laboratory measurements of samples of oil films taken from the sea. Thin films (thickness from fractions to hundreds of microns) are detected visually by their color manifestation [9, 10]. Of course, such visual assessments are very rough and did not take into account the variety of oil types, observation geometry, lighting conditions, thickness heterogeneity of the oil film, evaporation of light oil fractions, the influence of the atmosphere and waves. The identification of films in the ultraviolet (UV) region of the spectrum occurs due to an increase in the reflection coefficient of the surface covered by the film relative to pure water, i. e. by evaluating contrast [11]. This approach makes it possible to register the thinnest films with thicknesses from 0.1 to $10 \mu\text{m}$, build maps of the spatial distribution of film thicknesses in relative units, but it does not contain regular algorithms for reconstructing thicknesses.

In addition to methods related to the detection of surface pollution and attempts to characterize it, there is another scientific direction associated with the retrieval of wave characteristics in slick from solar path images, for example [12, 13]. At the same time, it was recently shown that the film on the water surface also appears in the underwater image [14, 15] due to the change of wave slopes. Our first algorithm for estimating the slope variance in the case of slopes less than 20° by distortion of Snell's window border was proposed in [1]. Subsequently, based on a simplified model of the Snell's window [16], the first approbation of wind-wave frequency spectra retrieval for clean surface and film-covered surface was presented [17]. All developed models did not take into account the effects of light scattering in water. Here we also restrict ourselves by considering small depths neglecting light scattering. But in general, the effects of multiple scattering and absorption of light in water also affect the distortion of the Snell's window border, getting stronger with depth increase (Fig. 1, *c*).

Analytical relations between statistical moments of the image and roughness were obtained in [16] by converting Snell's window image to its binary form with two values of radiance: 0 and 1. But in practice, the proposed approach is difficult to perform physically, because image formation should be performed by scanning the sea surface with a

luminance meter at a constant angle during vertical immersion. Besides, image distortions will increase with the increasing optical path, as well as time delay also must be accounted.

Recently in paper [18], based on the binarity of Snell's window images, analytical expressions for the derivatives of image statistical moments were presented in paper [16]. Using them in the present paper, as well as Elfouhaily spectrum of wind-driven waves, Ermakov model of wave damping by a thin film, and Cox-Munk result for a thick oil film, we investigated the behavior of these moments with variations of wind, wave, and film parameters in the numerical experiment. To distinguish film influence from wind weakening having similar manifestations, a series of real underwater images demonstrating the changes in the spot structure with surfactant film shifting through the observed sea surface area were analyzed. The presented results allow us to show how Snell's window sensitivity can be useful in practice for detecting surfactant films with the help of optical recorders fixed under the buoys, for example.

2. Theory

2.1. Model of the instantaneous Snell's window image formed by non-scattered light

Despite the fact, that the model of instantaneous Snell's window image has been repeatedly presented earlier (see, for example, [1]), general formulas are necessary for further discussion and calculations, as well as conditions of their applicability are presented here too.

Start with describing the geometry of underwater vision by Snell's window border. The wavy sea surface is uniformly illuminated by unpolarized light (Fig. 2, *a*). The instant relief of wavy sea surface at a given time moment is described by the function of the sea surface displacements $\zeta(\mathbf{r})$ and slope vector $\boldsymbol{\eta}(\mathbf{r})$, which is the horizontal component of the unit normal \mathbf{N} to surface in point $\mathbf{r}_\Sigma = \mathbf{r}_0 + \zeta(\mathbf{r}_0, t)\mathbf{e}_z$ (Fig. 2, *a*). Here $\mathbf{r}_0(x_0, y_0)$ is a radius-vector of the projection of the point \mathbf{r}_Σ on a plane $z = 0$, \mathbf{e}_z is the unit vector of z – direction. Displacements are considered as a zero-mean, stationary, and homogeneous random process. Slopes are related to displacements through the equation $\boldsymbol{\eta}(\mathbf{r}_0) = \nabla\zeta(\mathbf{r}_0) / \sqrt{1 + (\nabla\zeta(\mathbf{r}_0))^2}$.

The water optical properties are characterized by the light attenuation coefficient c and the refractive index m . In general, the latter is a function of water temperature, salinity, and light wavelength. The first two dependencies are weak concerning the considered hydro-optical problem, and the latter can be eliminated if we use only one wavelength. In practice, this condition can be realized using a corresponding color filter. As a result, the refractive index m is fixed to the value of 1.335 at 532 nm as well penetrated light wavelength for clean waters. Water temperature and salinity dependences are neglected.

The underwater image is formed with an optical receiver which is placed at the point \mathbf{r}_r at the depth Z_r (Fig. 2, *a*) to collect the angular distribution of radiance $L(\mathbf{n})$ coming from the sea surface. The unit vector \mathbf{n} which is a horizontal component of the unit vector of the refracted light $\boldsymbol{\Omega}$. Radiance at required depth can be found using the method of the Green function [19] through the radiance of the refracted light on a plane $z = 0$, $L_0(\mathbf{r}, \mathbf{n})$. Here the simplest model of the Green function neglecting light scattering is applied. Also, one more simplification is used, namely an effective boundary condition for the radiance on the plane $z = 0$ which ignores the influence of displacements to light field structure below a surface, i. e. $\zeta(\mathbf{r}_0) = 0$ and $\mathbf{r}_\Sigma = \mathbf{r}_0$. In this case, the air-water interface is similar to a refracting flat-screen, and the calculations of light fields are greatly simplified. Then, assuming that the receiver is located at shallow depths, where light scattering in water can be neglected, the radiance of direct (not-scattered) light at a depth Z_r as a function of the horizontal component \mathbf{n} of the unit vector of the refracted light is expressed in the form

$$L(\mathbf{n}) = L_0\left(-\mathbf{n}Z_r / \sqrt{1-n^2}, \mathbf{n}\right) \exp\left\{-cZ_r / \sqrt{1-n^2}\right\}, \quad (1)$$

through the radiance of the refracted light L_0 at depth $z = 0$ in point $\mathbf{r}_0 = -\mathbf{n}Z_r / \sqrt{1-n^2}$:

$$L_0(\mathbf{r}_0, \mathbf{n}) = m^2(1 - R_F(\alpha(\mathbf{r}_0, \mathbf{n})))L_{sky}(\mathbf{n}_i(\mathbf{r}_0, \mathbf{n})), \quad (2)$$

where

$$\mathbf{n}_i(\mathbf{r}, \mathbf{n}) = m\mathbf{n} + \left[m\left(\sqrt{1-n^2} - m\boldsymbol{\eta}\right) - \sqrt{m^2\left(\sqrt{1-n^2} - m\boldsymbol{\eta}\right)^2 - (m^2-1)(1+\eta^2)} \right] \frac{\boldsymbol{\eta}}{1+\eta^2} \quad (3)$$

is the horizontal component of the unit vector of the incident light $\boldsymbol{\Omega}_i$, expressed in terms of the slope $\boldsymbol{\eta}(\mathbf{r}_0)$ and the direction of the refracted light \mathbf{n} ,

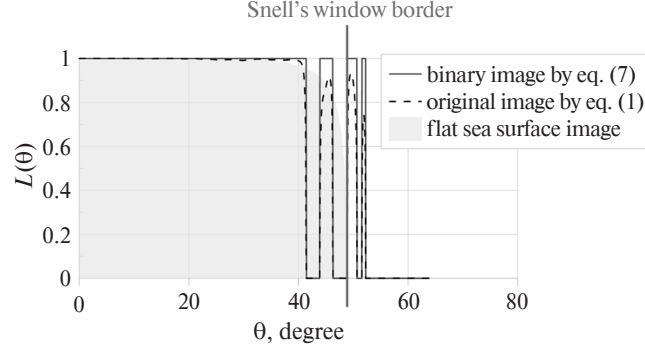


Fig. 3. Transformation of the original Snell's window image to a binary one.

for an arbitrary radial section of Snell's window. Below we considered similar sections, assuming the problem is one-dimensional.

2.2. Analytical models for the statistical moments of the Snell's window image

According to equation (3), directions of light falling on the sea surface from the right hemisphere are satisfied to condition

$$n_i \geq -1, \quad (8)$$

which means that light penetrates into the water through surface facets with slopes

$$\eta \geq \eta_0 = \frac{1}{\cos \vartheta} \left(\sin \vartheta - \frac{1}{m} \right). \quad (9)$$

Concerning mentioned above, the statistically average (accumulated) image $\langle L(\vartheta) \rangle$ and autocorrelation function of the image $K_L(\Delta\vartheta)$ can be calculated by the equations:

$$\langle L(\vartheta) \rangle = \int_{\eta_0(\vartheta)}^{\infty} L_b(\vartheta, \eta) P_1(\eta) d\eta, \quad (10)$$

$$K_L(\Delta\vartheta) = \langle L_b(\vartheta_1, \eta) L_b(\vartheta_2, \eta) \rangle = \int_{\eta_0(\vartheta_1)}^{\infty} \int_{\eta_0(\vartheta_2)}^{\infty} L_b(\vartheta_1, \eta) L_b(\vartheta_2, \eta) P_2(\eta_1, \eta_2) d\eta_1 d\eta_2. \quad (11)$$

Here $\Delta\vartheta = \vartheta_2 - \vartheta_1$ and functions $P_1(\eta)$ and $P_2(\eta_1, \eta_2)$ are the one-order and second-order probability density function (PDF) for slopes, respectively:

$$P(\eta) = \frac{1}{\sqrt{2\pi\sigma_x^2}} \exp \left[-\frac{\eta^2}{2\sigma_x^2} \right], \quad (12)$$

$$P_2(\eta_1, \eta_2) = \frac{1}{2\pi\sigma_x^2 \sqrt{1-R_\eta^2}} \exp \left[-\frac{\eta_1^2 - 2R_\eta \eta_1 \eta_2 + \eta_2^2}{2\sigma_x^2 (1-R_\eta^2)} \right], \quad (13)$$

where σ_x^2 is the slope variance, $R_\eta = R_\eta(\rho)$ is the normalized slopes autocorrelation function determined through the omnidirectional elevation spectrum $S(k)$ by Fourier transform

$$R_\eta(\rho) = \sigma_x^{-2} \int_0^{\infty} k^2 S(k) \cos\{k\rho\} dk, \quad (14)$$

$$\sigma_x^2 = \int_0^{\infty} k^2 S(k) dk, \quad (15)$$

$$S(k) = \int_{-\pi}^{\pi} k \Psi(k, \varphi) k d\varphi, \quad (16)$$

Here k is the wavenumber, φ is the wave direction relative to the wind, and $\Psi(k, \varphi)$ is the directional spectrum in polar coordinates. Angular radiance distribution L_b in equations (10) and (11) is written through variables ϑ and η on the basis of relations (3) and (5), highlighting η as a variable of integration.

Taking the integral in equation (10) leads to a solution via the error function:

$$\langle L(\vartheta) \rangle = \frac{1}{2} m^2 \operatorname{erfc} \left(\frac{\eta_0(\vartheta)^2}{\sqrt{2\sigma_x^2}} \right), \quad (17)$$

but subsequent using relation

$$\frac{d}{dx} \operatorname{erfc}(x) = -\frac{2}{\sqrt{\pi}} \exp\{-x^2\}, \quad (18)$$

allows to obtain an analytical solution for derivative of $\langle L(\vartheta) \rangle$ by the viewing angle ϑ :

$$\langle L(\vartheta) \rangle' = \frac{d\langle L(\vartheta) \rangle}{d\vartheta} = -\frac{1}{\sqrt{2\pi\sigma_x^2}} \left[1 + \frac{\sin(\vartheta)}{\cos^2(\vartheta)} \left(\sin(\vartheta) - \frac{1}{m} \right) \right] \exp \left\{ -\frac{1}{2\sigma_x^2} \cdot \frac{1}{\cos^2(\vartheta)} \left[\sin(\vartheta) - \frac{1}{m} \right]^2 \right\}. \quad (19)$$

An analytical expression for the second statistical moment is absent, but proceeding similarly, we obtained an expression for its second derivative:

$$\begin{aligned} K_L''(\Delta\vartheta) &= \frac{d^2 K_L(\Delta\vartheta)}{d\Delta\vartheta^2} = -\frac{1}{2\pi\sigma_x^2 \sqrt{1-R_\eta(\Delta\vartheta)^2}} \frac{1}{\cos^4(\Delta\vartheta/2)} \left[1 - \frac{\sin^2(\Delta\vartheta/2)}{m^2} \right] \times \\ &\times \exp \left\{ -\frac{\frac{2}{\cos^2(\Delta\vartheta/2)} \left[(1+R_\eta(\Delta\vartheta)) \sin^2(\Delta\vartheta/2) + (1-R_\eta(\Delta\vartheta)) \frac{1}{m^2} \right]}{2\sigma_x^2 (1-R_\eta(\Delta\vartheta)^2)} \right\}. \end{aligned} \quad (20)$$

These equations were used to analyze Snell's window image sensitivity to changes of sea roughness state due to wind straightening, fetch influence and surfactant films damping.

2.3. Spectrum for wind-driven waves

As follows from the previous equations, the calculation of the statistical moments of the image is possible by setting the wave characteristics, like the wind-driven wave spectrum $S(k)$. In the present paper an enough realistic Elfouhaily spectrum [20] which describes both gravity and capillary waves is used. It allows tracing the Snell's window image sensitivity to variations of the spectrum parameters in a wide range of wavenumbers.

2.4. Wave damping model for thin film

Surfactant films on the sea surface have a significant effect on the variability of waves and, as a result, on Snell's window structure. Their presence leads to partial damping of wind waves in the mm-cm ranges depending on visco-elastic characteristics and film thickness. The analytical models of thin films are well presented in the literature (see, for example, [21–23]). According to these models, the wind wave spectrum in slick represents as

$$S_{\text{slick}}(k) = S(k) / C(k), \quad (21)$$

where $C(k)$ is the spectral contrast. Below we used the Ermakov model [24], since it is quite physical and not overloaded by parameters. Only two parameters are used to describe the film: elasticity E and coefficient of surface tension σ . Applicable for winds less than 7 m/s, the selected model satisfactorily describes the experimental data for gravity-capillary waves with wavenumbers less than 1 rad/cm and has been repeatedly used to interpret the results of radar sensing of wind waves in film slicks.

2.5. Wave damping model for thick film

Due to the lack of a reliable model of a thick film, empirical results by Cox-Munk [13] are applied. According to their observations of a thick oil slick, the total slope variance decreases by a factor of 2–3 in comparison with a clean water surface. In the present paper the maximal factor was used for calculating the corresponding boundary wavenumber k_{\max} above which the spectrum was taken to be zero.

3. Results

Variations in statistical moments of the image in presence of surfactant film

Thin films are often found as a result of prolonged oil spill spreading or refueling accidents, or also may be associated with urban pollution. Therefore, below we consider films with typical corresponding parameters: two values of elasticity ($E = 5 \text{ mN/m}$ and $E = 20 \text{ mN/m}$) and two values of surface tension ($\sigma = 40 \text{ mN/m}$ and $\sigma = 75 \text{ mN/m}$). Their influence on the slope spectrum of wind-driven waves for wind speeds, V , of 3 m/s and 6 m/s is shown in Fig. 4. The lower value of speed corresponds to the beginning of wave generation and higher one describes the case of well-developed sea state without wavebreakings. Besides, this speed range is suitable for the application of the chosen thin-film model.

As it can be seen from Fig. 4, the wave spectrum is suppressed in presence of surfactant film. Corresponding boundary wavenumbers for every wind speed defines by film elasticity. The surface tension influence is negligible in most cases, but it becomes faintly noticeable for the least elastic films at the highest wind speeds (case of $V = 6 \text{ m/s}$, $E = 5 \text{ mN/m}$, $\sigma = 75 \text{ mN/m}$).

Spectrum changes are manifested in Snell's window structure and its statistical moments (Fig. 5). Accumulated images for a clean sea surface and film-covered one significantly differ (Fig. 5, *a*, at the top). Wind strengthening leads to distortion of the Snell' window border due to the occurrence of facets with bigger slopes, observed at bigger zenith angles. At the same wind, surfactant film reduces distortion due to capillary wave suppression and, as a result, facets with large slopes disappear. But, under certain conditions, the accumulated image of Snell's window may look the same for a clean surface at a lower wind speed (case of $V = 3 \text{ m/s}$ in Fig. 5, *a*) and for a film-covered surface at a higher wind speed (case of $V = 6 \text{ m/s}$, $E = 20 \text{ mN/m}$, and $\sigma = 75 \text{ mN/m}$). Distinguishing such situations will be considered in the Discussion section below using real Snell's window images.

The next two figures (Fig. 5, *a*, at the middle and bottom) demonstrate the border distortions with film parameter variations. As it can be seen, the noticeable sensitivity depends on the film elasticity for all considered wind speeds. The lowest sensitivity is observed to variation of surface tension at low wind speed. At high wind speeds, sensitivity becomes barely noticeable for larger surface tension, as a consequence of small spectrum variations (see Fig. 4). Generally, this situation is well known from the point of view of the interaction of film and wind-driven waves, but in application to the considered hydro-optical problem, it was necessary to challenge.

The considered cases of the thin-film manifestation are even more noticeable in the differentiated accumulated image as shown in Fig. 5, *b*. Estimates of the area under the curves $\langle L(9) \rangle'$ in relation to the wind speed and film parameter variations show that films with less elasticity lead to narrowing on average by 22 %, with more elasticity – by 30 %. Additional narrowing at low winds (3–5 m/s) at the level of 2% gives an increase in surface tension from 40 to 75 mN/m, and contribution increases to 4–6 % at winds of more than 5 m/s.

Further possible changes in the statistical moments of the image with surfactant film thickening were traced by cutting off wave spectrum at wavenumber 10 rad/m (wavelength 60 cm) following observations of Cox-Munk [13] and were calculated for two wind speeds (Fig. 5, at the top, black lines). Obviously, a thick film has a much more significant effect than a thin one. But, as it can be seen, an ambiguous situation may arise similar to those considered above for thin films. Perhaps, this is a drawback associated with the lack of a theoretical model and film parameters, although this situation is quite explainable. Therefore, the obtained result made us think on how to distinguish similar situations in practice.

Well noticeable variations of the autocorrelation function of the image, or rather its derivative, determined by expression (20), are presented in Fig. 6 for two wind speeds and films with different characteristics. Due to the presence

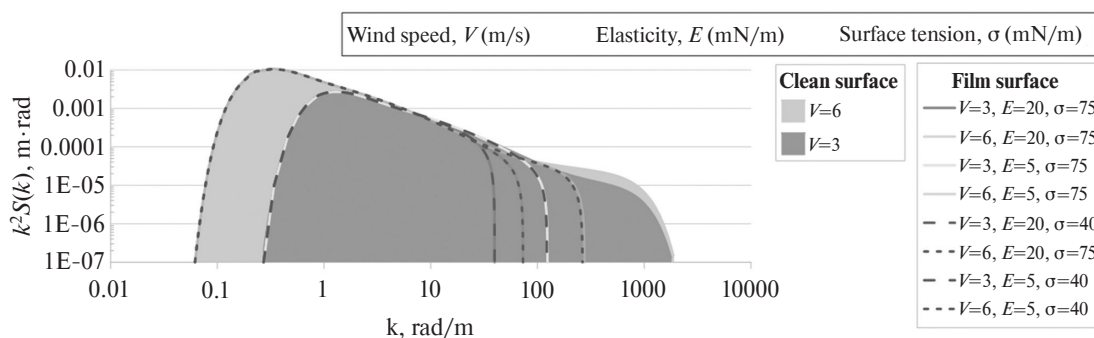


Fig. 4. The Elfouhaily spectrum of wave slopes at two wind speeds for clean surface and surface covered by thin films with different viscoelastic characteristics (see legend).

of an analytical relationship between it and the correlation coefficient of slopes, there is a chance to solve the inverse problem – to restore the wave spectrum, including a case of surfactant film presence. The solution to this problem on the example of the two-dimensional images will be presented in the next paper.

Variations in statistical moments of the image for undeveloped wind-driven waves

In contrast to the previous case, the variability of the image statistical moments was considered in connection with sequential cutting off the long-wavelength part of the spectrum, simulating the conditions of fetch-limited waves. In real conditions, such a situation can occur near curve coastline.

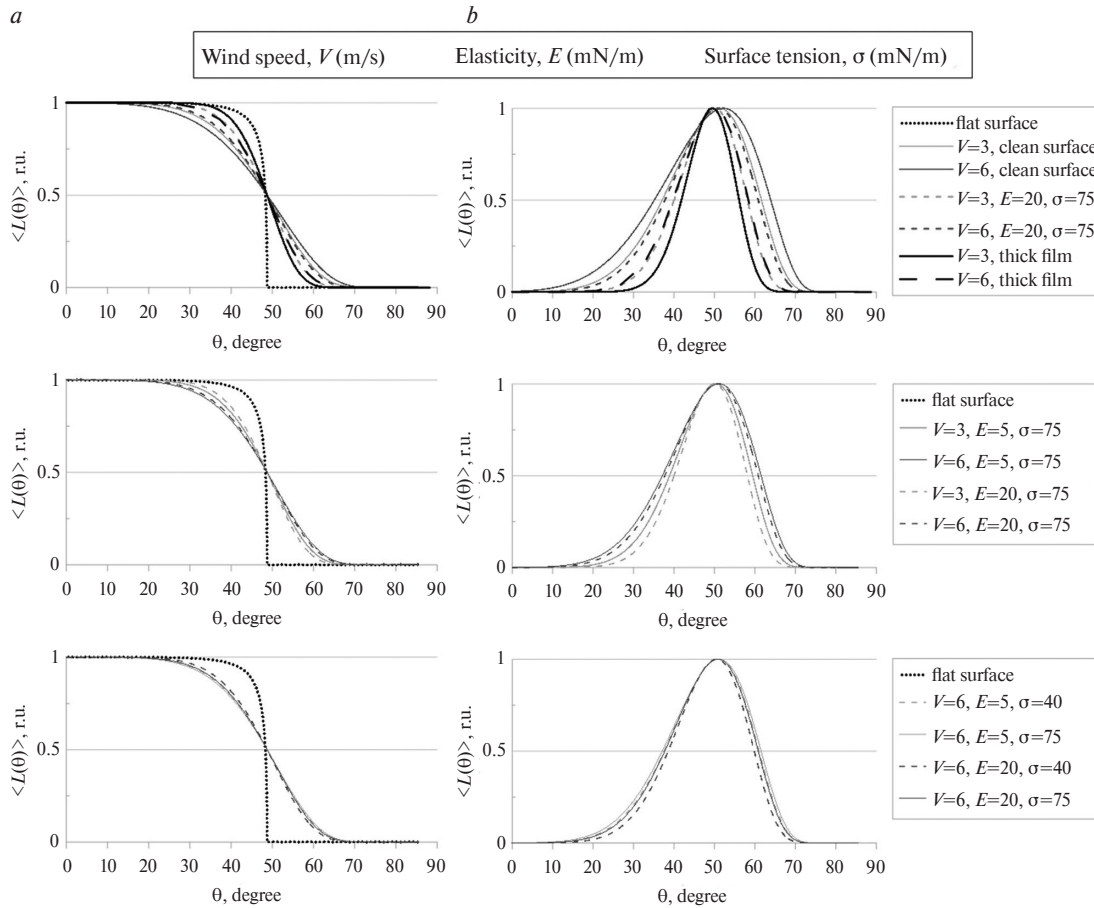


Fig. 5. Normalized accumulated images of Snell's window (a) and absolute value of their derivative (b) for a clean sea surface and surface covered by films for two wind speeds (parameters are indicated in legend).

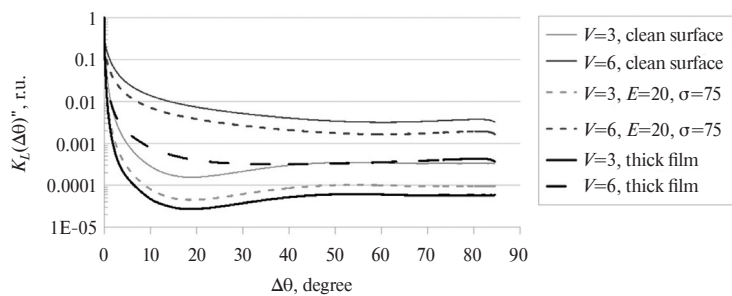


Fig. 6. Normalized double derivative of the autocorrelation function of the image for a clean sea surface and film-covered surface (see parameters in legend) for two wind speeds.

The Elfouhaily spectrum includes the inverse age of waves Ω_c , which depends on the dimensionless fetch for the energy containing waves and characterizes the degree of wave underdevelopment. An example of wave spectra for six values Ω_c from 0.84 (fully developed waves) to 5 (“young” waves) for the wind speed of 6 m/s is shown in Fig. 7. It can be seen, that in the case of young waves, the spectrum contains energy containing waves with lengths of 6 m (1 rad/m). Their absence leads to a slight decrease in the surface slopes (the slope variance decreases by 15–20 %) and, as a result, to a narrowing of the accumulated image and decreasing area under its derivative by about the same percentage (Fig. 8). More noticeable changes with wave development are registered by the derivative of the image correlation function (Fig. 9). Thus, for young waves, correlations rapidly weaken, the characteristic scale of correlations tends to the size of a single spot formed by the shortest waves in the mm range. As waves develop, the correlations increase, and the function tends to the same one discussed earlier.

The considered example emphasizes that despite the observed sensitivity of the considered statistical moments to wave variations, it is not enough to rely on anyone criterion, or one statistical moment, for a reliable conclusion about the cause of wave variability.

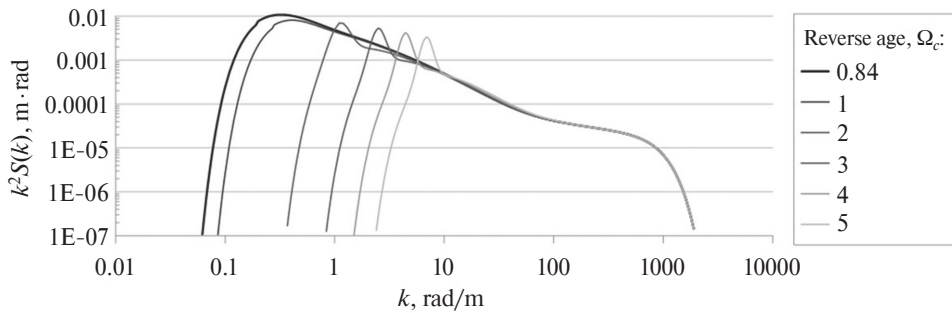


Fig. 7. The slope spectrum of undeveloped wind waves for the wind speed of 6 m/s and six values of reverse ages: from 0.84 (fully developed waves) to 5 (“young” waves).

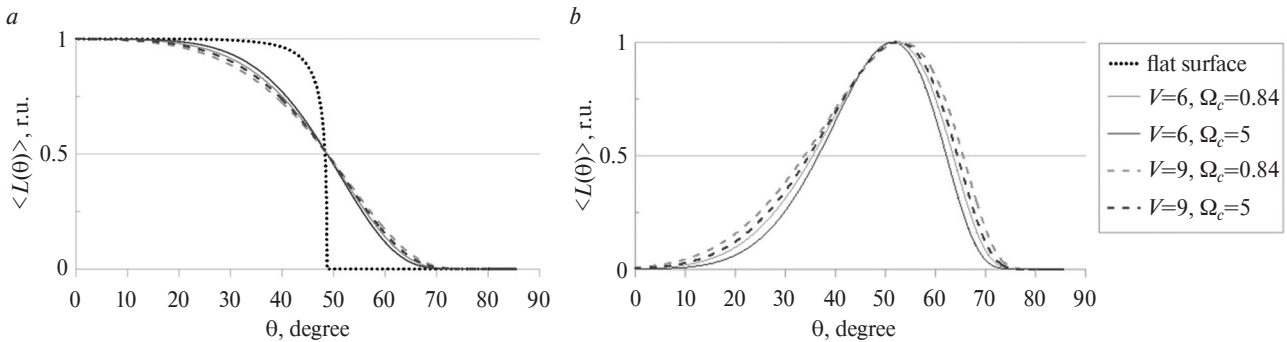


Fig. 8. Normalized accumulated images of the Snell’s window (a) and absolute value of their derivative (b) for fully developed ($\Omega_c = 0.84$) and “young” ($\Omega_c = 5$) wind waves at two wind speeds of 6 m/s and 9 m/s.

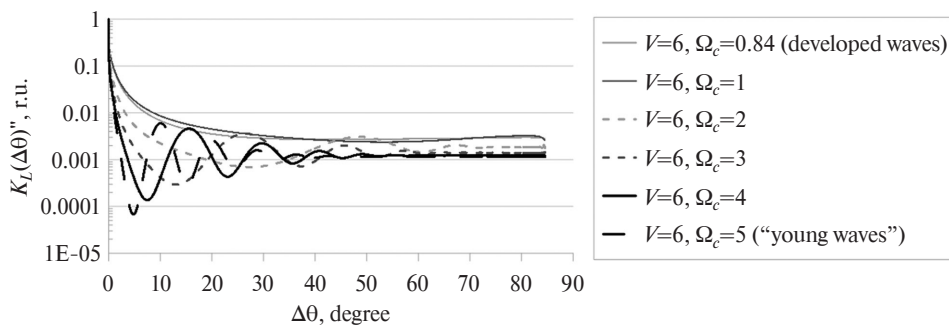


Fig. 9. Normalized absolute value of the double derivative of Snell’s window images for fully developed ($\Omega_c = 0.84$) and “young” ($\Omega_c = 5$) wind waves at two wind speeds of 6 m/s and 9 m/s.

4. Discussion

Of course, it would be interesting to trace the influence of films with known thicknesses on the considered statistical moments, but the corresponding reliable models for damping wind waves in a wide range of thicknesses are unknown. However, the presented variability of statistical moments of the Snell's window images for thin and thick films showed the principal theoretical possibility of its distinguishing. One may decide that in practice film detection can be confused, for example, with local wind weakening. Under specific conditions, this situation can take place, probably, but in general, these processes are separable when analyzing video recording of the Snell's window. Fig. 10 shows a series of frames from a video file of the Snell's window registered from a small depth of 1.5 m. Wind speed was about 3–4 m/s. The first image (Fig. 10, *a*) corresponds to a clean sea surface. After 5 s film covered the right half of the Snell's window where spots became larger (Fig. 10, *b*). Then, after the next 17 s, film covered all visible area and only big spots remained (Fig. 10, *c*). Demonstrated variations were related with the arrival of a film artificially created by spilling vegetable oil at a distance of about 200 m. Under wind shifting, spreading film occurs into the field of view of the underwater optical system after some time. The thin film on the front edge of the slick leads to gradual damping of capillary waves with the disappearance of small spots far from the border and the combining small spots into larger ones near border (Fig. 10, *b*). The subsequent passage of slick with a thicker central part leads to further smoothing of wavy surface and reducing distortion of Snell's window border (Fig. 10, *c*). After that, variations did not change for 10 minutes while the main part of the slick passed through the field of view. Then we watched how the slick leave the sighting area for 1 minute (Fig. 10, *d*, *e*).

Based on these examples, it is easy to imagine a slightly different situation, when at the initial moment of time the wind was weak and the surface was clean. After some time, the wind became noticeably stronger, and a film shifted into the field of view (cases “ $V=3$, clean surface” and “ $V=6$, $E=20$, $\sigma=75$ ” in Fig. 5, for example). As a result, small and most distant from the Snell's border spots, determined by capillary waves, were transformed into larger ones due to the damping of these waves by the film with the simultaneous development of longer gravity-capillary waves due to the wind strengthening. At the same time, the position of the new enlarged spots relative to the border did not change due to the sufficiency of the slopes. As a result, the statistically average images for these two cases are close. Therefore, as the considered example of real Snell's window images (Fig. 10) shows, the use of important information about size, quantity, and position of spots in every frame of time series should help in distinguishing ambiguous cases.

At the end of this section, let's consider another close case, namely, how to distinguish wind weakening from surfactant film presence. The point is that the weakening of the wind has a pulsating nature, wind never “turns off” instantly. The time of wind weakening is much longer than film damping time. Moreover, while the wind is weakening, capillary waves continue to exist, which means that many small spots remain. Therefore, changes in wind characteristics

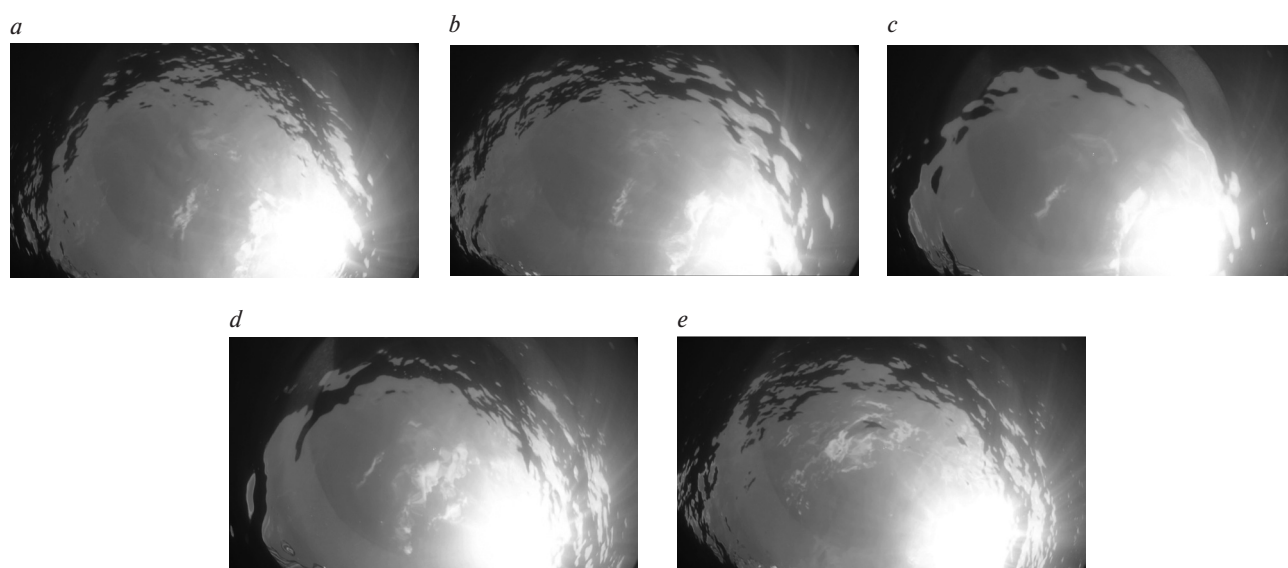


Fig. 10. Variations in a structure near Snell's window border due to surfactant film shifting through a field of view of the underwater camera from the right side to the left one: clean surface (*a*), film covered the right half of the Snell's window (*b*), film covered all visible area (*c*), film covered the left half of the Snell's window (*d*), and film left visible area (clean surface again) (*e*).

or near-surface hydrophysical processes occur at significantly longer times and they have diverse manifestations. This means that if Snell's window survey is carried out regularly with some discreteness in time, then this approach will make it possible to distinguish wind weakness from slicks or maybe various near-surface processes.

5. Conclusion

The presented paper demonstrates the results of studying sensitivity of underwater images of the sky (Snell's window) to variations of wind-driven waves and influence of surfactant films. This investigation was carried out on the example of the Elfouhaily wave spectrum, the Ermakov model of damping wave spectrum by a thin film, and the Cox-Munk empirical results on decreasing the slope variance of wind-driven waves in presence of thick oil film.

Based on simulation results, we establish clear sensitivity of some statistical moments of the image, like statistically average image, autocorrelation function of the image, and their derivatives. Useful information on wave statement is encoded in them differently. We found that the most significant changes are associated with the most elastic films. Variations in the surface tension do not lead to important manifestations in the images. The undeveloped waves are also manifested in the structure of spots near the Snell's window border, especially when analyzing the correlation characteristics of the image. At the same time, ambiguous situations were revealed when the observed statistical moments are similar for different intensities of waves. To resolve this situation, it is not enough to rely on only one criterion or statistical moment, it is necessary to involve additional information. Quite a lot of information can be obtained from the analysis of a series of sequential images. The considered example of real Snell's window images shows that the use of important information about size, quantity, and position of spots in every frame of time video series should help in distinguishing ambiguous cases.

The obtained results can be useful in the development of underwater monitoring systems in the coastal zone or inland waters based on buoys.

6. Funding

This research was supported by the Russian foundation of basic research (Grant No 19-35-60034). The data of field measurements used in section D were obtained during the expedition under the RSF project No 18-77-10066.

Литература

1. Мольков А.А., Долин Л.С. Определение характеристик ветрового волнения по подводному изображению морской поверхности // Известия РАН. Физика атмосферы и океана. 2012. Т. 48, № 5. С. 617—630.
2. Byfield V. Optical remote sensing of oil in the marine environment, Doctoral Dissertation. University of Southampton, 1998. 302 p.
3. Fingas M. The challenges of remotely measuring oil slick thickness // Remote Sensing. 2018. V. 10(2). P. 319. doi: 10.3390/rs10020319
4. Leifer I., Lehr W.J., Simecek-Beatty D., Bradley E., Clark R., Dennison P., Wozencraft J. State of the art satellite and airborne marine oil spill remote sensing: Application to the BP Deepwater Horizon oil spill // Remote Sensing of Environment. 2012. V. 124. P. 185—209. doi: 10.1016/j.rse.2012.03.024
5. Мольков А.А., Капустин И.А., Ермошкин А.В., Ермаков С.А. Дистанционные методы определения толщины плёнок нефти и нефтепродуктов на морской поверхности // Современные проблемы дистанционного зондирования Земли из космоса. 2020. Т. 17, № 3. С. 9—27 doi: 10.21046/2070-7401-2020-17-3-9-27
6. Goodman R.H. Simple remote sensing system for the detection of oil on water // Environmental Studies Research Funds, Report Number 098. Research Department, Esso Resources Canada Ltd, Calgary, Alberta, Canada, 1988, 6—9.
7. Clark R.N., Swayze G.A., Leifer I., Livo K.E., Lundeem S.A. Method for Qualitative Mapping of Thick Oil Using Imaging Spectroscopy. United States Geol., Survey, 2010.
8. Massaro A., Lay-Ekuakille A., Caratelli D., Palamara I., Morabito F. C. Optical performance evaluation of oil spill detection methods: thickness and extent // IEEE transactions on instrumentation and measurement. 2012. V. 61(12). P. 3332—3339. doi: 10.1109/TIM.2012.2210336.
9. Bonn Agreement. *Aerial Surveillance Handbook*. Expanded edition produced and renamed as the Aerial Operations Handbook in 2008. 65 p.
10. NOAA, Dispersant Application Observer Job Aid. National Oceanic and Atmospheric Administration, Washington DC, 2007.
11. Grüner K., Reuter R., Smid H. A new sensor system for airborne measurements of maritime pollution and of hydrographic parameters // GeoJournal. 1991. 24(1). P. 103—117.

12. Cox C., Munk W. Measurement of the roughness of the sea surface from photographs of the sun's glitter // *J. Opt. Soc. Am.* 11954. 44. P. 838—850.
13. Kudryavtsev V., Myasoedov A., Chapron B., Johannessen J., Collard F. Joint sun-glitter and radar imagery of surface slicks // *Remote Sens. Environ.* 2012. 120. P. 123—132.
14. Мольков А.А., Долин Л.С. О возможности регистрации пленок ПАВ на взволнованной водной поверхности средствами подводного видения // Труды международной конференции «Современные проблемы оптики естественных вод». 2015. Т. 8. С. 219—224.
15. Molkov A.A. Manifestation of surfactant films in underwater solar path images: numerical experiment // *Appl. Opt.* 2021. V. 60(14). P. 4190—4190. doi: 10.1364/AO.428100
16. Вебер В.Л. Использование явления полного внутреннего отражения света для диагностики морского ветрового волнения // *Изв. вузов. Радиофизика.* 2017. Т. 60, № 1. С. 530—540.
17. Molkov A.A., Dolin L.S., Kapustin I.A., Sergievskaya I.A., Shomina O.V. Underwater sky image as remote sensing instrument of sea roughness parameters and its variability // *Proceedings of SPIE Remote Sensing. V. 9999. Remote Sensing of the Ocean, Sea Ice, Coastal Waters, and Large Water Regions, 2016, 99991D, 2016.*
18. Molkov A.A. Retrieval of slope spectrum of sea roughness by Snell's window imagery: theory and numerical experiment (one-dimensional sea roughness) // *Proc. SPIE11529, Remote Sensing of the Ocean, Sea Ice, Coastal Waters, and Large Water Regions 2020, 115290C (20 September 2020), 2020.*
19. Долин Л.С., Левин И.М. Справочник по теории подводного видения. Л. : Гидрометеиздат, 1991. 230 с.
20. Elfouhaily T., Chapron B., Katsaros K., Vandemark D. A unified directional spectrum for long and short wind-driven waves // *J. Geophys. Res.* 1997. 102(C7). P. 15781—15796.
21. Grodsky S.A., Kudryavtsev V.N., Makin V.K. Evaluation of the influence of surface films on short wind waves and the characteristics of the boundary layer of the atmosphere // *Phys. Oceanogr.* 2001. V. 11(6). P. 495—508.
22. Левич В.Г. Гашение волн поверхностно-активными веществами. I // *Журнал экспериментальной и теоретической физики.* 1940. Т. 10(11). С. 1296—1304.
23. Cini R., Lombardini P.P. Damping effect of monolayers on surface wave motion in liquid // *J. Colloid Interface Sci.* 1978. 65. P. 387—389.
24. Ермаков С.А., Сергеевская И.А., Гуцин Л.А. Затухание гравитационно-капиллярных волн в присутствии нефтяной пленки по данным лабораторных и численных экспериментов // *Известия РАН. Физика атмосферы и океана.* 2012. Т. 48, № 5. С. 631—639. doi: 10.1134/S000143381204007X

References

1. Molkov A.A., Dolin L.S. Determination of wind roughness characteristics based on an underwater image of the sea surface. *Izv. Atm. Ocean. Phys.* 2012, 48, 552—564.
2. Byfield V. Optical remote sensing of oil in the marine environment, Doctoral Dissertation. University of Southampton, 1998. 302 p.
3. Fingas M. The challenges of remotely measuring oil slick thickness, *Remote sensing*, 2018, 10(2), 319. doi: 10.3390/rs10020319
4. Leifer I., Lehr W.J., Simecek-Beatty D., Bradley E., Clark R., Dennison P., Wozencraft J. State of the art satellite and airborne marine oil spill remote sensing: Application to the BP Deepwater Horizon oil spill. *Remote Sensing of Environment*, 2012, 124, 185—209. doi: 10.1016/j.rse.2012.03.024
5. Molkov A.A., Kapustin I.A., Ermoshkin A.V., Ermakov S.A. Remote sensing methods for measuring the thickness of oil/oil products on the sea surface. *Sovremennye Problemy Distantionnogo Zondirovaniya Zemli iz Kosmosa.* 2020, 17 (3), 9—27 (in Russian).
6. Goodman R.H. Simple remote sensing system for the detection of oil on water. *Environmental Studies Research Funds, Report Number 098. Research Department, Esso Resources Canada Ltd, Calgary, Alberta, Canada*, 1988, 6—9.
7. Clark R.N., Swayze G.A., Leifer I., Livo K.E., Lundeem S.A. Method for qualitative mapping of thick oil using imaging spectroscopy. *United States Geol., Survey*, 2010.
8. Massaro A., Lay-Ekuakille A., Caratelli D., Palamara I., Morabito F. C. Optical performance evaluation of oil spill detection methods: thickness and extent, *IEEE transactions on instrumentation and measurement.* 2012, 61 (12), 3332—3339. doi: 10.1109/TIM.2012.2210336
9. Bonn Agreement. *Aerial Surveillance Handbook.* Expanded edition produced and renamed as the Aerial Operations Handbook in 2008. 65 p.
10. NOAA, Dispersant Application Observer Job Aid, *National Oceanic and Atmospheric Administration*, Washington DC, 2007.

11. Grüner K., Reuter R., Smid H. A new sensor system for airborne measurements of maritime pollution and of hydrographic parameters. *GeoJournal*. 1991, 24 (1), 103—117.
12. Cox C., Munk W. Measurement of the roughness of the sea surface from photographs of the sun's glitter. *J. Opt. Soc. Am.* 1954, 44, 838—850.
13. Kudryavtsev V., Myasoedov A., Chapron B., Johannessen J., Collard F. Joint sun-glitter and radar imagery of surface slicks. *Remote Sens. Environ.* 2012, 120, 123—132.
14. Molkov A.A., Dolin L.S. On possibility of registration of surfactants on sea surface by means of underwater vision system. *Proceeding of VIII International Conference «Current Problems in Optics of Natural Waters»*. 2015, 8, 219—224 (in Russian).
15. Molkov A.A. Manifestation of surfactant films in underwater solar path images: numerical experiment. *Appl. Opt.* 2021, 60(14), 4190—4190. doi: 10.1364/AO.428100
16. Weber V.L. Use of the phenomenon of total internal light reflection for diagnostics of sea wind waves. *Radiophys. Quantum Electronics*. 2017, 60, 475—484.
17. Molkov A.A., Dolin L.S., Kapustin I.A., Sergievskaya I.A., Shomina O.V. Underwater sky image as remote sensing instrument of sea roughness parameters and its variability. *Proceedings of SPIE Remote Sensing, Volume 9999, Remote Sensing of the Ocean, Sea Ice, Coastal Waters, and Large Water Regions*, 2016, 99991D, 2016.
18. Molkov A.A. Retrieval of slope spectrum of sea roughness by Snell's window imagery: theory and numerical experiment (one-dimensional sea roughness). *Proc. SPIE11529, Remote Sensing of the Ocean, Sea Ice, Coastal Waters, and Large Water Regions 2020, 115290C (20 September 2020)*, 2020.
19. Dolin L.S., Levin I.M. Theory of underwater vision. *Leningrad, Gidrometeoizdat*, 1991. 230 p (in Russian).
20. Elfouhaily T., Chapron B., Katsaros K., Vandemark D. A unified directional spectrum for long and short wind-driven waves. *J. Geophys. Res.* 1997, 102(C7), 15781—15796.
21. Grodsky S.A., Kudryavtsev V.N., Makin V.K. Evaluation of the influence of surface films on short wind waves and the characteristics of the boundary layer of the atmosphere. *Phys. Oceanogr.* 2001, 11(6), 495—508.
22. Levich V.G. Wave damping by surfactant films. I. *Soviet Physics – JETP*. 1940, 10, 1296—1304 (in Russian).
23. Cini R., Lombardini P.P. Damping effect of monolayers on surface wave motion in liquid. *J. Colloid Interface Sci.* 1978, 65, 387—389.
24. Ermakov S.A., Sergievskaya I.A., Gushchin L.A. Damping of gravity-capillary waves in the presence of oil slicks according to data from laboratory and numerical experiments. *Izv. Atmos. Ocean. Phys.* 2012, 48, 565—572. doi: 10.1134/S000143381204007X